Additive Manufacturing 68 (2023) 103503

Contents lists available at ScienceDirect

Additive Manufacturing

journal homepage: www.elsevier.com/locate/addma

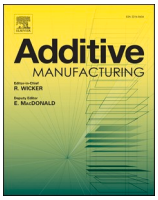

Cyclic behaviour and microstructural evolution of metastable austenitic stainless steel 304L produced by laser powder bed fusion

Miroslav Šmíd [a,b,*], Daniel Koutný [c], Kateřina Neumannová [a], Zdeněk Chlup [a], Luboš Náhlík [a,b], Michal Jambor [a]

[a] Institute of Physics of Materials, Czech Academy of Sciences, Žižkova 22, Brno 616 62, Czech Republic
[b] CEITEC IPM, Institute of Physics of Materials, Žizkova 22, Brno 616 62, Czech Republic
[c] Faculty of Mechanical Engineering, Institute of Machine and Industrial Design, Brno University of Technology, Technická 2896/2, Brno 616 69, Czech Republic

ARTICLE INFO

Keywords:
Cyclic behaviour
Laser powder bed fusion
Stainless steel
Strain induced phase transformation
Chemical segregation

ABSTRACT

It has been documented that the hierarchical character of microstructure produced by laser powder bed fusion (L-PBF) is the key to superior mechanical properties. Especially important is a fine cell microstructure possessing heterogeneous distribution of dislocation density and alloying elements. Despite multiple studies that have investigated the effect of such L-PBF structure on the stress-strain response during monotonic loading, just a few investigations were devoted to cyclic behaviour. The present study delivers an insight into the cyclic behaviour of L-PBF processed metastable austenitic stainless steel 304L and its relation to the observed microstructure evolution and strain-induced martensitic transformation (SIMT). The combination of scanning electron microscopy (SEM) and transmission electron microscopy (TEM) observations, and feritscope measurements enabled to follow the onset of strain-induced martensite (SIM) nucleation and underlying dislocation microstructure evolution. The cyclic behaviour consisted of initial cyclic softening regardless of subjected strain amplitude. Afterwards, milder cyclic softening or saturation stage followed until a final failure was characteristic for the tests held at low strain amplitudes ($\varepsilon_a \leq 0.5\%$). The third fatigue life stage, cyclic hardening, was recorded during fatigue tests held at $\varepsilon_a > 0.5\%$. The excellent cyclic strength of stainless steel 304L is a direct consequence of cell microstructure containing high dislocation density walls and elemental microsegregation, which effectively inhibit dislocation motion. Cyclic softening was linked with cyclic strain localization into slip bands of decreased dislocation density and heavily altered dislocation cell walls. These bands have been observed for the first time in L-PBF-processed metals. This microstructural feature seems to be a variant of persistent slip bands (PSBs), a typical dislocation arrangement observed in conventionally produced materials subjected to cyclic loading. PSBs present the areas of intensive cyclic plasticity where the SIMT preferentially occurs upon further cycling. The increasing α'-martensite volume fraction, accompanied by a formation of intermediate ε-martensite and deformation twinning, resulted in recorded cyclic hardening. The martensite nucleation sites are strongly determined by the underlying cell microstructure, in terms of cell walls dislocation density and chemical segregation, which is tightly related to utilized L-PBF process parameters. The present findings indicate a possible opportunity to control the magnitude of the SIMT susceptibility by fine-tuning of the L-PBF process parameters and consequently tailoring the cyclic behaviour.

1. Introduction

Additive manufacturing (AM) has been attracting the attention of industry and academia already for more than three decades. Since then, the technology has developed from a rapid prototyping tool to a convenient manufacturing solution for the industrial applications, where a final product benefits from the advantages such as unprecedented design freedom, single-step nature of the process, flexibility and lately an option of multi-material fabrication [1–4]. Currently, AM is considered to be a significant disruptive manufacturing technique with great perspective, especially in the upcoming digitalized industry era with a strong accent to the final product individualization [5–7]. Numerous AM techniques have emerged to meet diverse requirements originating from various feedstock materials, applications, build sizes

* Corresponding author at: Institute of Physics of Materials, Czech Academy of Sciences, Žižkova 22, Brno 616 62, Czech Republic.
E-mail address: smid@ipm.cz (M. Šmíd).

https://doi.org/10.1016/j.addma.2023.103503
Received 22 December 2022; Received in revised form 5 March 2023; Accepted 15 March 2023
Available online 21 March 2023

and many other important aspects [8–10]. The powder bed fusion techniques, such as L-PBF, have emerged as one of the front-runners for metal AM due to versatility and a combination of precision and possible geometry complexity. The process is based on the melting of powder in highly localized manner by a fine high energy source with subsequent abrupt cooling rates in range of 10^3 - 10^8 K.s^{-1}. A unique solidification structure, characteristic of the majority of additive manufactured (AM) alloys [11–13], is formed under such conditions. The obtained structure is in a highly non-equilibrium state leading to the formation of unique heterogeneous hierarchical microstructure, which offers the superior combination of high strength and ductility [11,14–16] impossible to achieve by casting, powder metallurgy or wrought processes [17]. The main reason for the attractive combination of mechanical properties was attributed to the complex multi-scale nature of structure, while especially the fine cell structure of grain interior presents numerous obstacles for dislocation motion by high dislocation density walls. It has been proven by Kong et al. [18] that the cell microstructure originates from the melt pool solidification and underlying chemical microsegregation processes are of the same origin as the dendritic microstructures originating from casting and welding. Consequently, the chemical segregation closely follows the cell walls and it has been confirmed by Smith et al. [19] to further inhibit the dislocation motion by the coherent internal stresses stemming from chemical misfits and the elastic modulus variations between alloying element enriched and depleted regions within nano-scale of the cell size.

Stainless steels (SS) belong to one of the most frequently used material class for AM because of fairly low powder feedstock costs, corrosion resistance, already broad AM processing parameters knowledge base and excellent combination of strength and ductility. Especially, the high ductility offers an important structural damage tolerance to possible processing-related defects in a build, such as lack of fusion pores, gas pores and keyholing, preventing unexpected failure. The deformation behaviour of SSs, and metals generally, can vary significantly and is determined by the stacking fault energy (SFE) of a given steel. The SFE value is predominantly related to the chemical composition and actual temperature at the moment of deformation. Typically, the deformation is dominated by dislocation slip for the alloys with SFE $>$ 45 mJ.m^{-2} or with prevalent deformation twinning, i.e. twinning induced plasticity (TWIP) effect, while SFE ranges between 20 and 45 mJ.m^{-2}. In the case of the alloys possessing SFE $<$ 20 mJ.m^{-2}, the transformation-induced plasticity (TRIP) effect will occur to a significant extent. Therefore, the SFE has direct implications on active deformation mechanisms and consequently on the stress-strain response under monotonic loading [20–22] and on the character of cyclic behaviour upon fatigue loading, which was documented by multiple studies [23–28] performed on conventionally processed SSs and high manganese steels. The L-PBF counterparts, containing the intricate microstructure, experience frequently more difficult activation of various deformation mechanisms due to high structural heterogeneity in terms of dislocation density, internal stresses and chemical microsegregation. Under tensile loading, the stress-strain response and underlying deformation microstructure have been studied extensively and are well understood [11,14,29–33]. However, cyclic behaviour presents a more difficult situation due to dynamic character of the loading and its well-known sensitivity of overall fatigue performance on structural defects, which are frequently introduced into as-built structure during the L-PBF process. Moreover, the back-and-fro dislocation movement in complex dislocation cell substructure presents a difficult task for microstructural characterization while depending just on as-built and post-mortem observations. Despite several recently published studies [34–39], the evolution of dislocation microstructure or typical dislocation alignment features resulting from fatigue loading were not characterized up to now. It is vital to acquire detailed insight into microstructural evolution for a better understanding of the essential relation between the L-PBF processing parameters, as-built microstructure and cyclic behaviour. Such investigations can stimulate possible microstructural tailoring to improve the resistance to fatigue loading and, thus, the overall reliability of AM structures.

By performing cycle fatigue tests at various strain amplitudes, the present study aims to investigate the cyclic behaviour of metastable austenitic 304L SS and to follow the dislocation microstructural evolution accompanied by the formation of PSBs and subsequent SIMT. The microstructural evolution insight was provided by the series of interrupted fatigue tests held at the same strain amplitude. The comprehensive SEM and TEM observations complemented by feritscope measurements were able to characterize cyclic plasticity featured by pronounced cyclic strain localization and the effect of characteristic L-PBF solidification microstructure, namely cell structure and chemical microsegregation.

2. Experimental

2.1. Sample fabrication process

Nitrogen gas-atomized powder of 304L SS (Sandvik Osprey Ltd., United Kingdom) was used as a feedstock material for the L-PBF. The powder particles were fully dense with a bimodal distribution of round and irregular morphologies with small satellite particles attached as shown in Fig. 1a. The particle analysis was carried out by a laser diffraction particle size analyzer Malvern 2000 and characteristic values of the obtained size distribution are presented in Fig. 1a. Table 1 presents the chemical composition of powder. Powder flow properties were characterized by the Hall flow test and by the tapped density analysis resulting in values of 16.3 s / 50 g and 59.5%, respectively.

The L-PBF process was carried out by an SLM 280HL facility (SLM Solution Group AG, Germany) equipped with a Yb-fiber laser with maximum nominal power of 400 W and laser spot diameter of approximately 80 μm with a Gaussian intensity profile. During the fabrication, the chamber was constantly purged with nitrogen gas to minimize oxygen content and a square-shaped build plate of size 100 × 100 mm^2 was kept heated at 100 °C. The L-PBF process was performed using a stripe pattern with 67° layer-to-layer rotation. The laser was operated at power of 235 W, scanning speed of 790 mm.s^{-1}, hatch distance of 120 μm and layer thickness of 50 μm. The calculated volumetric energy density was 50 J.mm^{-3}, which is significantly lower than values proposed by other studies investigating 304L or 316 L SS [30,40–42]. The laser delay time between each layer was 30 s. The blocks with dimensions of 13×13×82 mm^3 were printed horizontally and subsequently machined into the final tensile and fatigue cylindrical specimens with the building direction (BD) perpendicular to the loading direction (LD). The chemical composition of the as-built specimen, shown in Table 1, was measured by arc/spark optical emission spectrometry (OES). Based on these results the SFE value was calculated to be 27 mJ.m^{-2} using the empirical equation proposed by Schramm and Reed [43].

2.2. Material characterization

The as-built microstructure characterization and porosity measurement were performed using the cross-sections of specimen heads. The samples were extracted along two planes to obtain a comprehensive microstructural description - perpendicularly to the stress axis and along the BD – LD plane. The samples were mechanically ground by SiC papers with increasing grit size. Prior to the porosity measurement, the samples were mechanically polished by a sequence of diamond pastes containing fine particles of 3, 1 and ¼ μm in size. The porosity measurements were performed by an Olympus DSX1000 digital microscope on a 3.5 × 3.5 mm^2 area with subsequent image processing by the ImageJ software [44]. Subsequently, the high surface quality for electron back-scattered diffraction (EBSD) was achieved by electrolytic polishing done by a Struers LectroPol-5 using a solution of 600 ml methanol, 360 ml ethylene glycol monobuthyl ether and 60 ml perchloric acid under voltage 35 V for 40 s at temperature 15 °C. Characteristic

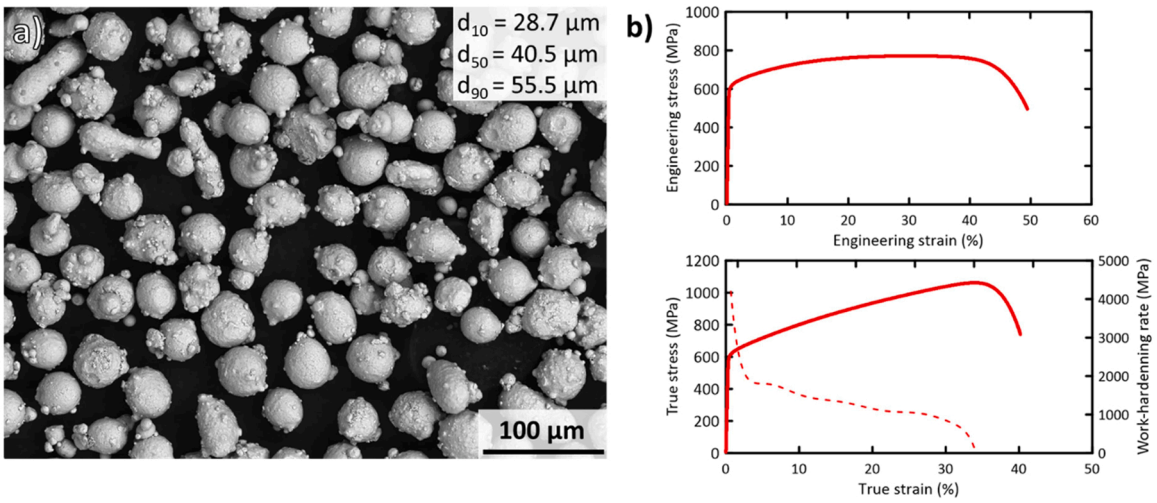

Fig. 1. SEM micrograph of 304L powder (a) and (b) engineering and true stress-strain curves in as-built condition.

Table 1
Chemical composition of 304L steel powder and as-built specimens (in wt%).

	C	Cr	Ni	Mn	N	S	P	Si	Fe
Powder	0.02	18.7	8.3	1.5	0.14	0.006	0.023	0.73	Bal.
As-built	0.03	19.41	8.18	1.4	0.15	0.004	0.027	1	Bal.

solidification structure after L-PBF was revealed by electrolytic etching using a 10% dilution of oxalic acid in deionized water under conditions of 5 V for 45 s. The temperature of the etchant was kept at 12 °C. Post-mortem microstructural characterization was carried out on the samples sectioned from specimen gauge areas along the BD - LD plane.

Electron microscopy observations were carried out by a TESCAN LYRA 3 XMU field emission gun scanning electron microscope (SEM), equipped with an Oxford Instruments Symmetry electron backscatter diffraction (EBSD) detector. The acquired raw EBSD data were processed by the open-source software MTEX [45]. TEM observations were performed on the samples of 3 mm diameter extracted from the sections of specimen gauge area extracted by an electron discharge cutting machine along the BD-LD plane. After mechanical grinding till reaching the sample thickness of approximately 80 µm, the final step of double jet electrolytic thinning was carried out in a solution of 95% acetic acid and 5% perchloric acid using a Struers TenuPol-5 device. Dislocation structure observation was performed by a JEOL JEM-2100 F scanning transmission electron microscope (S/TEM) operating at 200 kV. Nano-scale chemical heterogeneity of as-built microstructure was characterized by an image-corrected and monochromated FEI Titan-Themis S/TEM equipped with a Super-X EDS detector operated at 300 kV. Low magnification observation of dislocation substructures was carried out by transmission mode of scanning electron microscopy (SEM-TE). These observations were performed on a thin sample, dedicated for TEM, by a detector situated underneath the examined TEM sample. The electron beam was held at 30 kV with beam current of 0.25 nA at working distance of 5.5 mm.

2.3. Feritscope measurement

Magnetic permeability measurements were performed using a Feritscope FMP30 to quantify the α′-martensite volume fraction in a representative volume. The measurements were carried out on electrochemically polished longitudinal (BD-LD) gauge area sections of fatigued specimens in 10 random spots, at least 3 mm away from a fatigue crack. Any traces of ferromagnetic phases (i.e. δ-ferrite or α′-martensite) weren't detected in as-built condition, thus, the measured values after cyclic loading can be fully attributed to SIM. Moreover, the feritscope measurements were compared with the phase fraction determined by EBSD. Since the measurements were in good agreement, the frequently used correction factor of 1.7 for feritscope readings [46,47] was not considered in this study. Therefore, the term of volume fraction of α′-martensite will be used for the feritscope measurement results.

2.4. Mechanical tests

Tensile test specimens with a gauge length of 35 mm and diameter of 6 mm were strained by a screw-driven testing machine ZWICK Z50 at the constant strain rate of 1 $mm.min^{-1}$. Stress–strain curves in both representations and work-hardening rate are shown in Fig. 1b. The as-built material exhibited an excellent combination of ductility (total elongation of 49%) and strength (yield and ultimate strength were 592 and 780 MPa, respectively) within a similar range to the previous studies [14,15,42,48,49]. Feritscope measurement revealed 4.6% of α′-martensite fraction outside of the necked area.

The fatigue specimens, with gauge area dimensions of 6 mm in diameter and 11 mm in length, were subjected to cyclic loading by an MTS 880 servo-hydraulic machine controlled by an electronic system. The fatigue specimen gauge area was ground by SiC papers and electrolytically polished by 1.5:5:100 vol ratio solution of nitric, perchloric acid and ethanol at voltage of 46 V and temperature of 0° ± 5 °C for 2 min. The applied force was measured by a load cell and an extensometer, attached to the specimen gauge area, was utilized to perform the tests in constant total strain regime. All tests were held in fully reversed mode ($R_\varepsilon = -1$) at constant strain rate of 2.10^{-3} s^{-1}. The number of cycles to failure was defined as the drop of the mean stress-to-stress amplitude ratio below the value − 0.1. Two series of cyclic tests were performed – tests held at the selected range of total strain amplitude ε_a (from 0.3% to 1%) and the series of tests held at $\varepsilon_a = 0.7\%$ interrupted at selected points of fatigue life ($N = 5$, 25, 50, 200, 400 and 600 cycles).

3. Results and discussion

3.1. Material

Fig. 2a depicts an etched as-built solidification structure. Optimized L-PBF parameters resulted in nearly fully dense samples with porosity of 0.05%. Lack of fusion pores were sporadically detected along the melt pool boundaries. The microstructure consisted of characteristic columnar grains with the preferential inclination along the BD following the dominant macroscopic thermal gradient during liquid solidification [50,51]. The characteristic microstructural feature was epitaxial grain growth across melt pool interfaces. Fig. 2b shows the EBSD band contrast map with highlighted high-angle grain boundaries (HAGBs) and numerous annealing twins interfaces which implies the partial relaxation of residual stresses during the melt pool solidification. An EBSD IPF map in the projection along the BD, Fig. 2c, shows the crystallographic nature of microstructure without any preferential texture. The epitaxial grain growth across the melt pool interfaces is evident while the dominant grain growth direction along the BD was typical for areas in melt pool centre line. Away from the melt pool centre, the columnar grains are locally inclined perpendicular to the melt pool interface curvature, following the local thermal gradients during solidification. In such cases, epitaxial growth across the melt pool interfaces of a certain grain fraction was provided by side-branching, as shown in Fig. 2d. The pole figures of the principal crystallographic planes (Fig. 2e) confirm the random nature of the as-built microstructure. The abrupt nature of the solidification process is reflected by the GND map, shown in Fig. S1a in Supplementary materials, where individual melt pools are recognizable due to higher values of GND along boundaries. The misorientation angle distribution of boundaries and interfaces within the area analyzed by EBSD, Fig. S1b, documents the frequent occurrence of annealing twins and numerous fine misorientations stemming from low-angle grain boundaries (LAGBs) defined in range of 2 – 15°. Within individual grains, the LAGBs define subgrain domains containing dislocation cells with similar crystallographic orientation.

A deeper insight into microstructure is presented by bright field STEM images, shown in Fig. 3. The grains consisted of the subgrain domains, with the average size in orders of a few micrometres, defined by LAGBs. The low misorientation angle between subgrain domains is proven by a slight decrease of contrast in several areas in Fig. 3b, stemming from a small deviation from the ideal diffraction condition. Furthermore, the subgrain domains contained the dislocation cell network with high dislocation density walls and low dislocation density cell interiors. Fig. 3b depicts the microstructure in perpendicular projection to the image plane of Fig. 3a and also several annealing twins. It is apparent that the cell microstructure was strongly columnar along $< 001 >$ crystallographic directions. The average cell diameter was 530 nm while the length was ranging from several to tens of micrometres. Due to high cooling rates during the L-PBF process, the cell substructure presents an ultrafine dendritic structure limited just to a single dendritic axis. Therefore, it is possible to use the following function between primary dendritic arm spacing λ_1 (in our study average cell size) and acting cooling rates ε, proposed by Katayama and Matsunawa [52]:

$$\lambda_1 = 80(\varepsilon)^{-0.33} \quad (1)$$

The calculated value $\varepsilon = 3.2 \times 10^6$ K.s^{-1} agrees with the typical values for L-PBF processed materials [34,35,53]. Consequently, the microstructure is highly heterogeneous in terms of dislocation density distribution and chemical microsegregation. The latter is documented

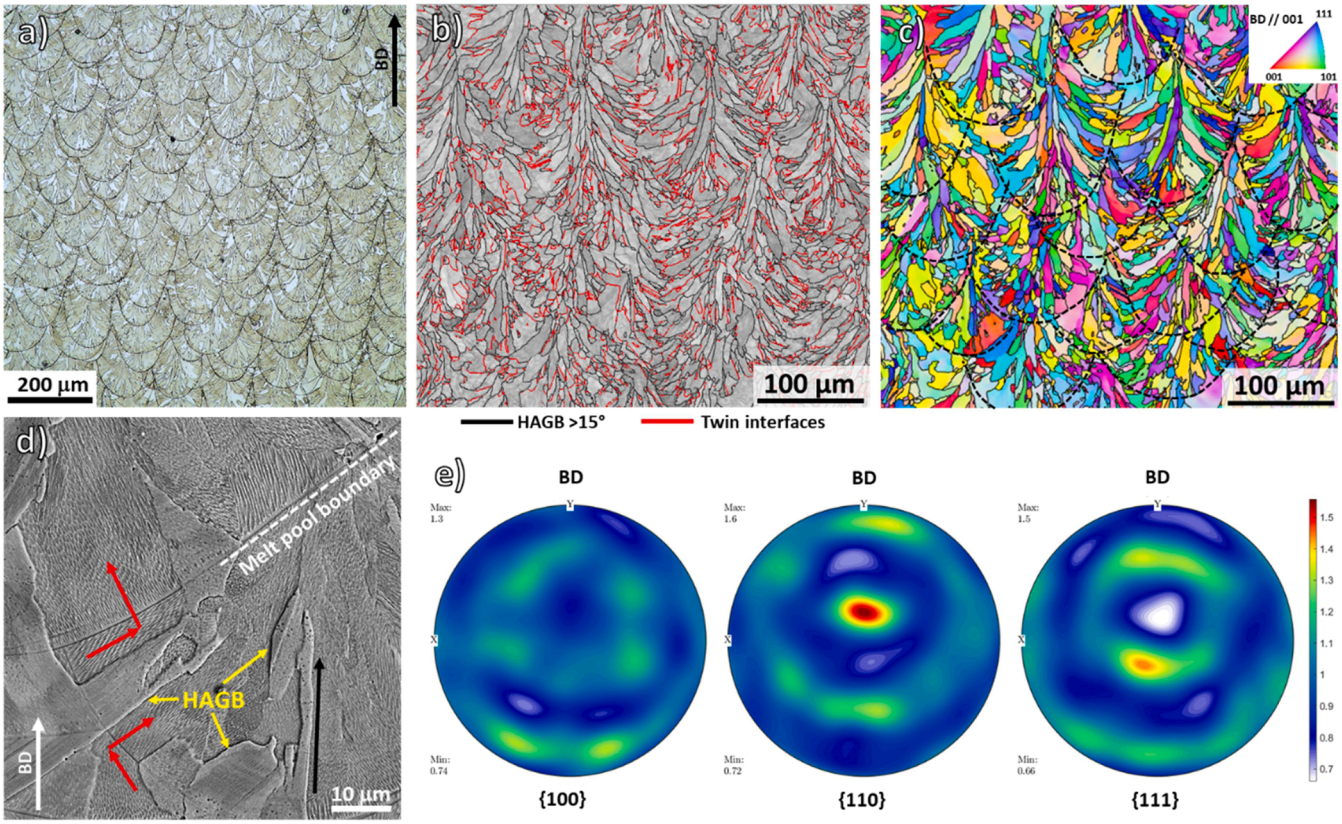

Fig. 2. As-built solidification structure of L-PBF 304L steel: a) light micrograph of etched structure with melt pool boundaries; b) band contrast map with high-angle grain boundaries (HAGB) highlighted by black and twin interfaces (red); c) IPF map in projection along the BD; d) SEM micrograph of melt pool boundaries with revealed HAGBs, cell substructure and evidence of side-branching (red arrows) and slender columnar grain growth in melt pool centreline (black arrow); e) pole figures of the principal crystallographic planes indicating fairly random crystallography.

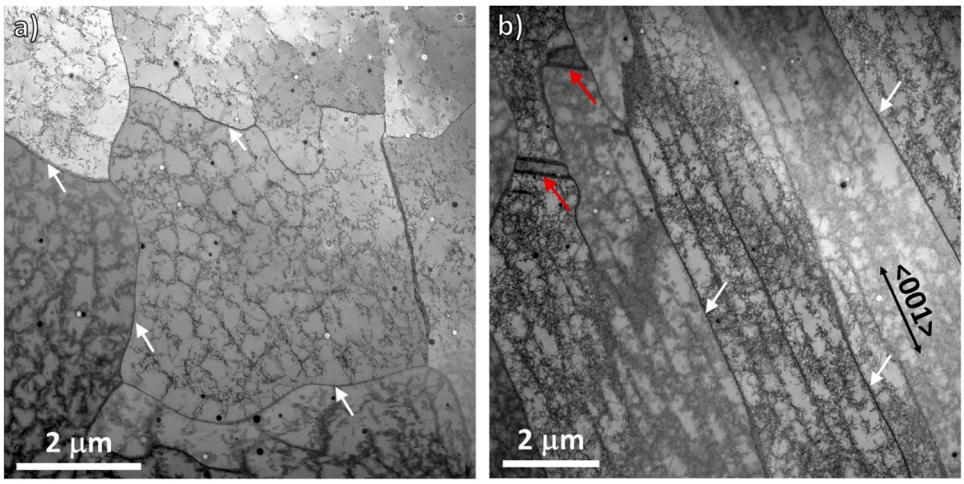

Fig. 3. Bright-field STEM images of as-built microstructure with pronounced subgrain boundaries (white arrows), annealing twins (red arrows) and cell dislocation substructure in projection where: a) cell growth is approximately perpendicular to the image plane; b) the cell growth occurs within the image plane along the shown <001> direction.

by STEM EDS mapping, shown in Fig. 4, indicating the segregation of alloying elements, for instance, Cr, Ni and Mn. The chemical inhomogeneities follow the cell walls which is apparent from STEM BF image. Furthermore, alloying and impurity elements such as O, Si and Mn are concentrated in fine oxide precipitates, most likely $MnSiO_3$, along the cell walls and LAGBs, visible also in Fig. 3b as fine particles. Similar microstructural features were documented in the previous TEM studies [54,55]. The chemical mapping also occasionally identified Al-rich particles, probably originating from powder contamination. The effect of oxide nanoparticles is still the topic of ongoing investigations, however, it has been reported that the strengthening effect via possible dislocation pinning mechanism is minor especially in comparison with the strengthening presented by dislocation cell structure [38,56]. The present precipitates are too large and with insufficiently low spacing to introduced a notable strengthening effect. On the other hand, it has been suggested that the oxide precipitates can present enhanced thermal stability of microstructure by serving as Zener-pinning points preventing the grain growth [57].

The heterogeneous and hierarchically structured material with described characteristics (HAGBs, twin interfaces, dislocation cell structure, fine oxides, chemical microsegregation) offers an excellent combination of high yield and ultimate strength with very good

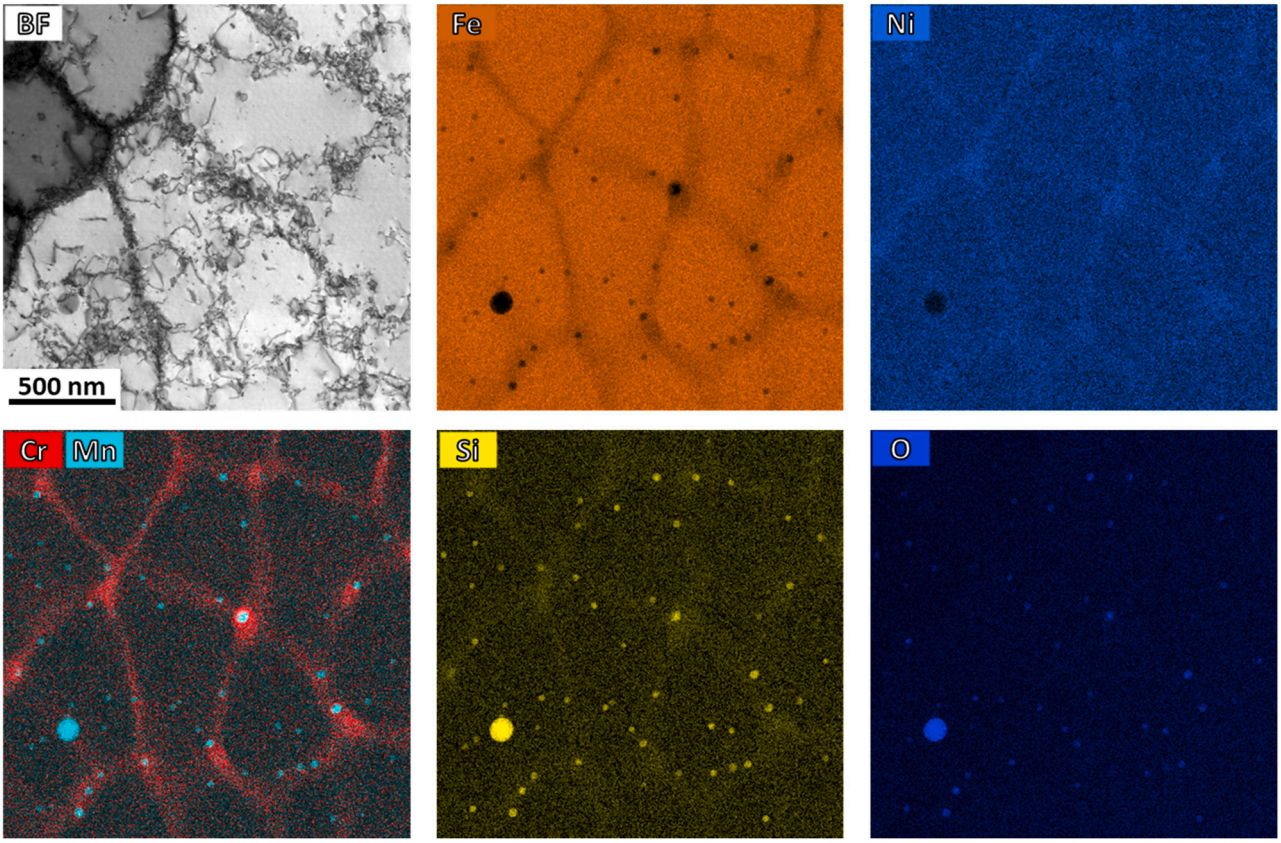

Fig. 4. STEM EDS mapping of selected elements. The Cr microsegregation coincides with dislocation cell walls as well as Mn- and Si-rich oxides distribution.

ductility, typical especially for face cubic centred (FCC) alloys fabricated by AM [14,16,41,42,58–60].

3.2. Cyclic stress-strain response

Cyclic behaviour was studied in a wide range of strain amplitudes ε_a and is summarized in Fig. 5. Cyclic softening/hardening curves, Fig. 5a, indicate pronounced initial cyclic softening which was characteristic for all tests while the length of this stage was dependent on ε_a. With the increasing number of cycles, the cyclic softening gradually diminished until saturation of cyclic response was reached. It needs to be noted that at $\varepsilon_a = 0.3\%$, the cyclic softening was mild and the saturation stage was not even reached, whereas strong and significantly shorter cyclic softening was recorded at $\varepsilon_a = 1\%$ followed by the saturation stage. Moreover, the cyclic tests at $\varepsilon_a \geq 0.5\%$ led to an occurrence of the third fatigue life stage, cyclic hardening. The magnitude of cyclic hardening was rising with increasing ε_a, namely with its plastic part ε_{ap}. The degree of cyclic softening and hardening presented by stress amplitude change $\Delta\sigma_a$ is plotted in Fig. 5b as a function of ε_a. The plot shows that the most pronounced cyclic softening was observed at $\varepsilon_a = 0.5\%$ and with further strain amplitude increase, this stage gradually got weaker. On the other hand, from $\varepsilon_a \geq 0.5\%$ the cyclic hardening increases. Interestingly, the cyclic hardening seems to reach its maximum at $\varepsilon_a = 0.8\%$. This is supported by the feritscope measurement (Fig. 5a) where a progressive increase of martensite content until $\varepsilon_a = 0.8\%$ was observed. The martensite volume fraction of about 10.5% appears to be the maximum achievable fraction induced by cyclic loading for this particular chemical composition and solidification structure originating from the selected processing parameters.

Fig. 5c presents cyclic behaviour of the specimen strained at $\varepsilon_a = 0.7\%$ till fracture ($N = 2044$) complemented with feritscope measurements carried out on the series of interrupted tests at a selected number of cycles ($N = 5$, 25, 50, 200, 400, 600). The feritscope measurement results show the kinetics of the SIMT in the course of fatigue life and with respect to the cyclic behaviour. The onset of SIMT occurred already after 50 cycles during the softening stage and accelerated with further cyclic straining. It seems that martensite volume fraction of 0.5% has already a noticeable effect on the cyclic behaviour, which is reflected by the onset of cyclic softening decline. Subsequently, the cyclic saturation is reached around $N = 500$ cycles where the estimated volume fraction of martensite is approximately 1%. The martensite nucleation rate progressively increased in the second half of fatigue life which can be directly linked with macroscopically observed cyclic hardening.

3.3. Microstructural characterization

3.3.1. Early fatigue life stage

Fig. 6 depicts the SEM-TE dislocation structures observation of the specimens used for the interrupted fatigue tests, which were already utilized for the feritscope measurement. The onset of cyclic straining is represented by the microstructure after 5 cycles. The dislocation cell structure was intact, however, distinct signs of ongoing cyclic strain localization along the primary slip system were identified in the majority of grains already after such short cyclic loading history. The stacking faults (SFs) were concentrated in high density within slip bands fully intersecting grains. The SFs, accompanied by partial dislocations, are depicted in a form of narrow lines due to the edge-on imaging condition given by specific grain crystallographic orientation with respect to the incident electron beam. Accompanying partial dislocations were predominantly concentrated around dislocation cell walls indicating the pronounced inhibiting effect. Additional 20 cycles ($N = 25$) led to further intensification of the cyclic strain localization. The number of slip bands do not change significantly but they were more distinguishable due to the continuing local modification of cell dislocation walls stemming from the interactions with mobile dislocations. This finding implies that a significant fraction of cyclic plasticity is localized within these evolving slip bands which is further supported by nearly intact dislocation cell walls in surrounding matrix. The corresponding micrograph and its inset show a grain with multiple slip bands along the highly inclined (111)-type slip system with respect to the foil plane. Due to this imaging condition, the areas of tangled partial dislocations within dislocation walls are visible as discontinuous bands. Moreover, this set of micrographs documents that the LAGBs do not present effective barriers for dislocation motion since the slip bands are transmitted into the neighbouring subgrain domain without any notable signs of dislocation accumulation. After $N = 50$ cycles, the first α′-martensite nuclei, accompanied presumably with SFs and intermediate ε-martensite, were observed within the well-developed slip bands, which were identified in the majority of grains at high frequency. It is important to note that the martensite nucleation was more frequent in grain interior than in grain boundary – slip band intersections. Further cyclic straining resulted in a more pronounced diversification of microstructure when cyclic saturation was reached and cyclic hardening start to emerge, as it is shown in micrographs from the test interruption at $N = 400$ cycles. At this stage, the slip bands can be characterized by strikingly lower dislocation density and severely modified or nearly diminished dislocation cell wall structure. The band appearance and also apparent function as a dislocation motion facilitator strongly resemble a dislocation alignment known from cyclically strained

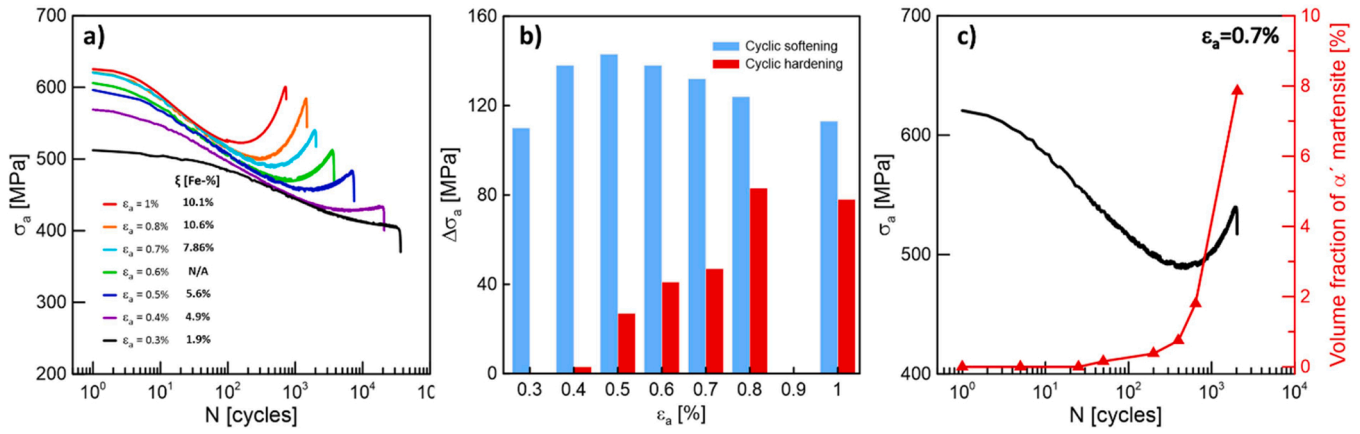

Fig. 5. Characterization of cyclic behaviour: a) stress amplitude σ_a vs. number of cycles with α′-martensite phase fraction acquired by feritscope measurement, b) magnitude of the cyclic softening and hardening stages as function of total strain amplitude, c) α′-martensite volume fraction evolution during fatigue life of the test held at $\varepsilon_a = 0.7\%$.

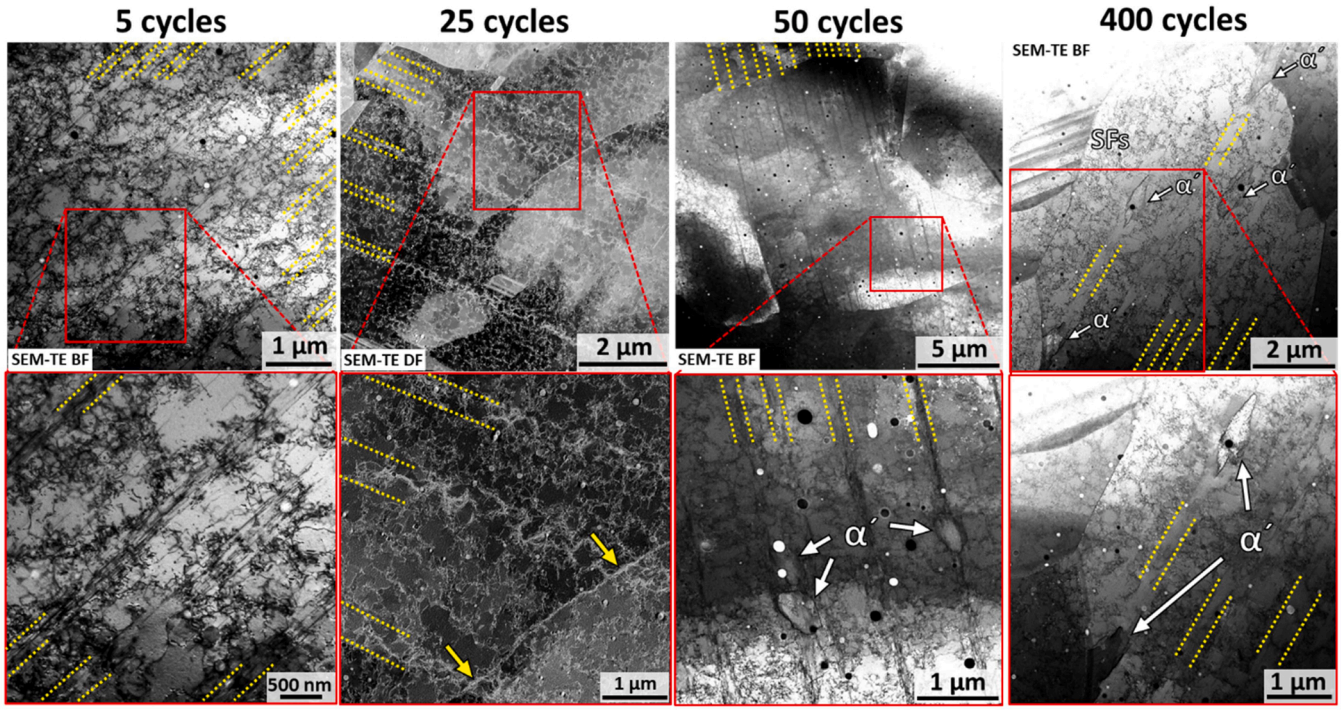

Fig. 6. SEM-TE observations representing dislocation microstructure evolution at initial stages of fatigue life under cyclic loading at $\varepsilon_a = 0.7\%$. The onset of PSBs formation as observed after 5 cycles, highlighted by yellow dotted lines. With further cycling the signs of cyclic strain localization gets more evident with increased frequency PSBs and development of their interior. PSBs are spanning across the whole grain neglecting LAGBs, shown by yellow arrows. The first α′-martensite nucleated within PSBs already after 50 cycles. Further cyclic loading led to significant decrease of dislocation density within the PSBs, as detected in the microstructure after 400 cycles.

conventional materials – PSBs. It seems that the unique L-PBF microstructure introduces a specific form of PSBs, shown in Fig. 6. Generally, the grain interior consisted of two distinctively different areas: i) the PSBs, where dislocation density dropped rapidly and numerous martensite islands were nucleated, and ii) outside of the PSBs which remained nearly intact in terms of cell structure and dislocation density.

The fatigue tests have shown that L-PBF 304L SS experienced the cyclic softening at the early stage of fatigue life, which is in a direct contrast to a brief cyclic hardening typical for conventional hot-rolled counterparts [61–65]. The principal reason can be attributed to the distinct difference in microstructure character originating from the unique nature of L-PBF - heterogeneous microstructure with complex-shaped grains containing high dislocation density distributed in a dislocation cell walls network [11], whereas the hot-rolled microstructure consisting of polyhedral grains with low dislocation density. The significant difference in initial microstructure will be inevitably reflected by the different cyclic stress response. In the case of a hot-rolled microstructure, a rapid dislocation density increase in grain boundary areas, stemming from overcoming intergranular plastic strain incompatibilities due to grain-to-grain misorientations, has been documented to be responsible for the initial cyclic hardening stage [63]. The following saturation and cyclic softening fatigue stages can be typically attributed to further dislocation matrix evolution featured by nucleation of PSBs, a low-energy dislocation configuration which enables to accommodate significantly higher amount of cyclic plastic deformation than the surrounding matrix [66–68]. The L-PBF microstructure presents significantly more difficult conditions for dislocation motion. Generally, the dislocation motion is strongly inhibited while crossing individual dislocation cell walls, which are considered to be effective soft barriers [11,17,18,34,56]. In order to overcome them, an increase in shear stress acting on a mobile dislocation is required. Therefore, AM materials exhibit significantly higher strength and simultaneously retain high ductility, since the dislocation motion is effectively impeded but not prevented. The main factors of superior strength have been studied thoroughly by Cui et al. [38,56] and Wang et al. [17]. The key impact was attributed to the Hall-Petch strengthening, dislocation strengthening and solid solution strengthening, the latter stemming from coherent internal stresses caused by solute alloying elements, such as Mn. These unique microstructural conditions have a notable implication on cyclic behaviour - the initial cyclic hardening stage is omitted, due to already high initial dislocation density, and the cyclic softening is typically observed as the first fatigue life stage [36,69,70]. The cyclic dislocation motion is not fully reversible in the majority of cases and therefore gradual dislocation arrangement evolution can be observed. The results of performed interrupted tests, shown in Figs. 5c and 6, present an evidence of the link between cyclic softening and the PSBs formation. As it has been documented by Lavenstein et al. [68] by in situ observations, the PSBs nucleate already after a few cycles, which agrees well with the slip bands found after 5 cycles, shown in Fig. 6. It is believed that several factors acting simultaneously determine the PSB nucleation sites, such as: i) local high stress concentrations induced by HAGB or oxide precipitates; ii) locally coarser cell size or cell wall with lower dislocation density and iv) feasible crystallographic orientation for dislocation slip. Such local fluctuation in a complex L-PBF microstructure can initiate the dislocation motion. Consequently, the continual to-and-fro dislocation motion caused by symmetric cyclic loading results in a high frequency of dislocation interactions with dislocation cell structure. For instance, dislocation annihilation and cell wall dislocation unpinning result in the gradual degradation of dislocation cell walls in terms of dislocation density at the sites of intersection with active slip planes. Moreover, Liu et al. [11] proposed that dislocation cell walls can act as additional dislocation source which can further increase dislocation activity and contribute to the cell walls degradation. Subsequently, these modified areas of microstructure are able to accommodate cyclic plasticity more easily than surrounding matrix, which is reflected by the nucleation of PSBs. The performed

electron microscopy observations suggest that PSBs nuclei occur simultaneously at several sites and progressively propagate across the whole grain as it has been experimentally evidenced by Lavenstein et al. [68]. At this point, the L-PBF microstructure can be regarded as a composite of a "hard" matrix with nearly unaffected dislocation cell wall structure and a certain volume fraction of mechanically "softer" areas where dislocation density decreased due to the intensive cyclic strain localization. It has been experimentally evidenced that PSBs can accommodate a substantially larger portion of plastic strain than the surrounding matrix [66,71], which can be regarded as the required prerequisite for the SIMT. The SIM was detected within emerging PSBs approximately from $N = 50$ cycles, as shown in Fig. 6. These observations were supported by the feritscope measurements, Fig. 5c, indicating 0.16% of α′-martensite. Such value reflects the very beginning of α′-martensite nucleation in preferential areas. The SIM presents another strengthening factor as an additional obstacle for mobile dislocations due to the FCC-BCC interfaces with difficult dislocation transmission and local internal stresses stemming from the phase transformation volume change of approximately 2.7% [72]. With further cyclic loading, the number of martensite nuclei keeps increasing which is reflected by the phase fraction increase between cycles 50 and 400, depicted in Fig. 5c. This microstructural evolution is accompanied by a notable effect on the cyclic softening weakening until reaching cyclic saturation. The following stage, cyclic hardening, can be linked with the rapid increase of α′-martensite phase fraction recorded from cycle 400 till fracture stemming from martensite islands growth, which will be further characterized in the following section.

In summary, the observation of microstructure at various moments of the early fatigue life stages has shown that an L-PBF microstructure presents effective barriers for dislocation motion with a beneficial effect on fatigue resistance. The cyclic loading induces the progressive degradation of dislocation cell structure in the intersection areas with emerging PSBs, a pronounced dislocation motion facilitator, reflected macroscopically by the initial cyclic softening behaviour. The further cyclic plastic straining is accommodated in PSBs, where consequently the SIMT is triggered. The strengthening effect of α′-martensite is responsible for the recorded change in cyclic behaviour towards the cyclic hardening.

3.3.2. *Post-mortem microstructure*

Fig. 7 depicts micrographs of the microstructure cyclically strained at $\varepsilon_a = 0.3\%$ till fracture. The majority of observed grains contained numerous PSBs along the primary slip system, as shown in Fig. 7a. The PSBs interior was featured by distinctively lower dislocation density compared to micrographs from interrupted cyclic test at $N = 400$. Generally, the PSBs interior presents the areas favourable for dislocation motion and, thus, promotes the localization of cyclic plasticity, which consequently results in the SIMT evidenced by numerous α′-martensite nuclei, shown in Fig. 7. The SIM was observed in a form of irregular islands with rugged-shaped boundaries. Sporadically, the favourably oriented grains with PSBs along multiple slip systems were found, as presented in Fig. 7b. In such cases, the PSB intersections were found to be feasible α′-martensite nucleation sites with intensive cyclic plasticity, resembling the shear bands intersection-mediated nucleation described by Olson and Cohen [73] as significant α′-martensite nucleation sites. The martensite morphology and position within and along PSBs indicate the strain-induced nature of martensitic transformation. Fig. 7c shows a grain with complex-shaped α′-martensite nuclei and also severely altered dislocation cell structure within PSBs. Moreover, observed narrow planar lattice defects in vicinity of the martensite phase were identified as fine bands of ε-martensite by selected area electron diffraction (SAED). It is assumed that ε-martensite acts as intermediate phase in the active martensitic transformation sequence which is typical for 304L and similar SSs [73,74]. Liu et al. [11] has proposed, based on the conducted in situ TEM observations, that dislocation cell walls can be regarded as traps for passing partial dislocations leaving mobile just one from the pair. This can potentially lead to the formation of ε-martensite (an occurrence of unpaired partials on every second plane) or deformation nanotwins (while unpaired partials occur on planes consecutively). Also deformation twinning was confirmed by performed TEM observations, as shown in the following micrographs.

With increasing ε_a of cyclic loading, a stronger cyclic strain localization is necessary to accommodate an additional cyclic plastic strain. The gradual evolution of deformation microstructure after cyclic loading at $\varepsilon_a = 0.5\%$ and 0.7% is shown in Fig. 8. The frequency of PSBs within grains is generally higher than at $\varepsilon_a = 0.3\%$ and the SIMT is more intensive, as shown in Fig. 8b,d and e. Martensite islands are significantly larger and their growth is not constrained just to PSBs. Moreover, the grains with PSBs or SFs along multiple slip systems (see Fig. 8c) were observed more frequently and the features of additional deformation mechanism, such as deformation twinning, begin to occur especially at $\varepsilon_a = 0.7\%$ (see Fig. 8d). The inset of Fig. 8e shows an increased dislocation density observed in α′-martensite, which indicates a certain degree of cyclic plastic sharing with the austenitic matrix. Since α′-martensite possesses higher critical shear stress, the strengthening effect of such cyclic plasticity contribution is expected. A similar effect can be attributed to annealing twins inherited from cyclic thermal history typically experienced during the L-PBF process. Fig. 8 f depicts multiple annealing twin interfaces occupied by a high density of dislocations and stacking faults. The ability to hinder dislocation motion and

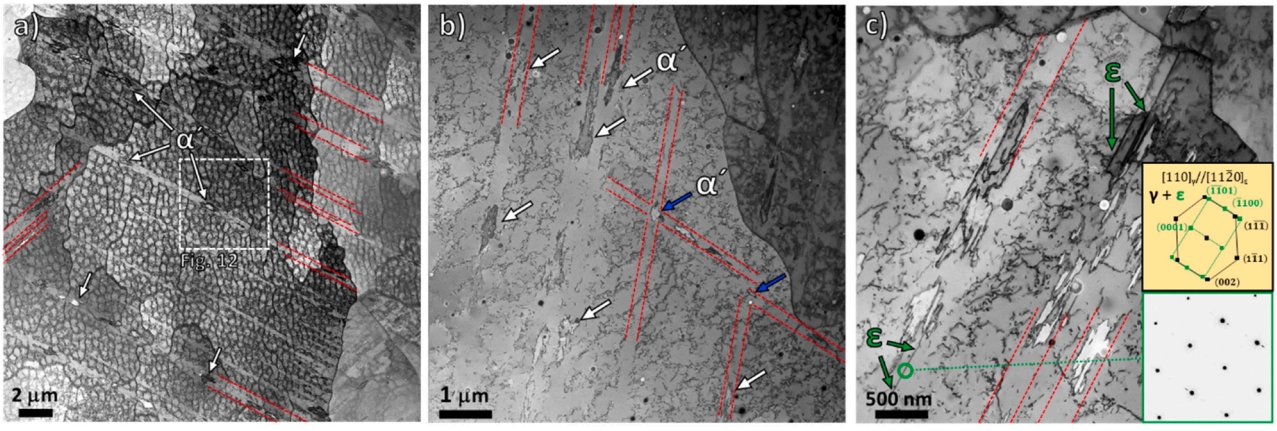

Fig. 7. STEM-BF micrographs of post-mortem microstructure after cyclic straining at $\varepsilon_a = 0.3\%$: a) Apparent cyclic strain localization into PSBs along primary slip system (red dashed line) decorated by numerous strain-induced α′-martensite nuclei (white arrows); b) A grain with PSBs aligned along two active slip systems. α′-martensite nucleation occurred at the PSBs intersections (blue arrows); c) The evidence of ε-martensite appearance inside of PSBs confirmed by SAED (yellow circle).

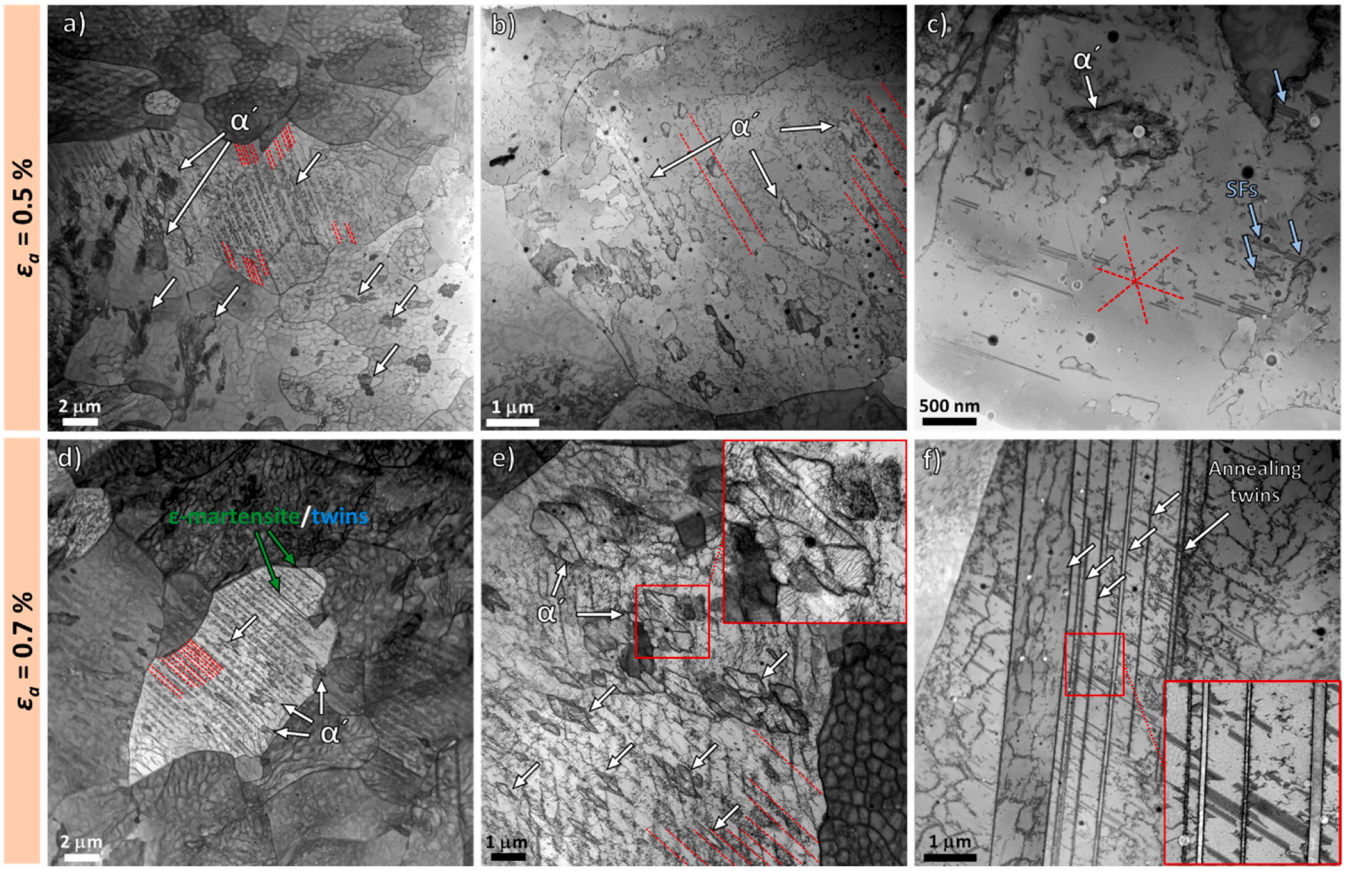

Fig. 8. STEM-BF micrographs of post-mortem microstructure after cyclic straining at $\varepsilon_a = 0.5\%$ and 0.7%: a) A grain with multiple PSBs containing large martensite islands (shown by white arrows); b) Distinct modification of dislocation structure by dislocation motion apparently concentrated into the bands (red dashed lines) with numerous α′-martensite; c) Grain region with three active slip systems (red dashed lines) and with frequent SFs (light blue arrows) inhibited by underlying cell substructure; d) The evidence of increasing PSB density with increasing ε_a of cyclic loading with notable appearance of deformation twinning and ε- and α′-martensite inside a single grain; e) Intensive SIMT in PSBs and neighbouring matrix. Detail depict high dislocation density within α′-martensite; f) Dislocation and SFs hindering along the annealing twin interfaces.

difficult slip transmission, into twin interior has been mentioned previously by Jang et al. [75] and is further supported in Fig. 8 f inset detail.

Fig. 9 presents typical microstructure, which underwent intensive cyclic plastic deformation upon loading held at $\varepsilon_a = 1\%$ accompanied by the significant cyclic hardening stage. The feritscope measurements, presented in the Section 3.2, have shown that the α′-martensite volume fraction was nearly similar to that identified after the cyclic test at $\varepsilon_a = 0.8\%$, which presumably indicates that other deformation mechanisms were required to contribute in extended scale to accommodation additional plastic deformation. Fig. 9a shows a low-magnification STEM

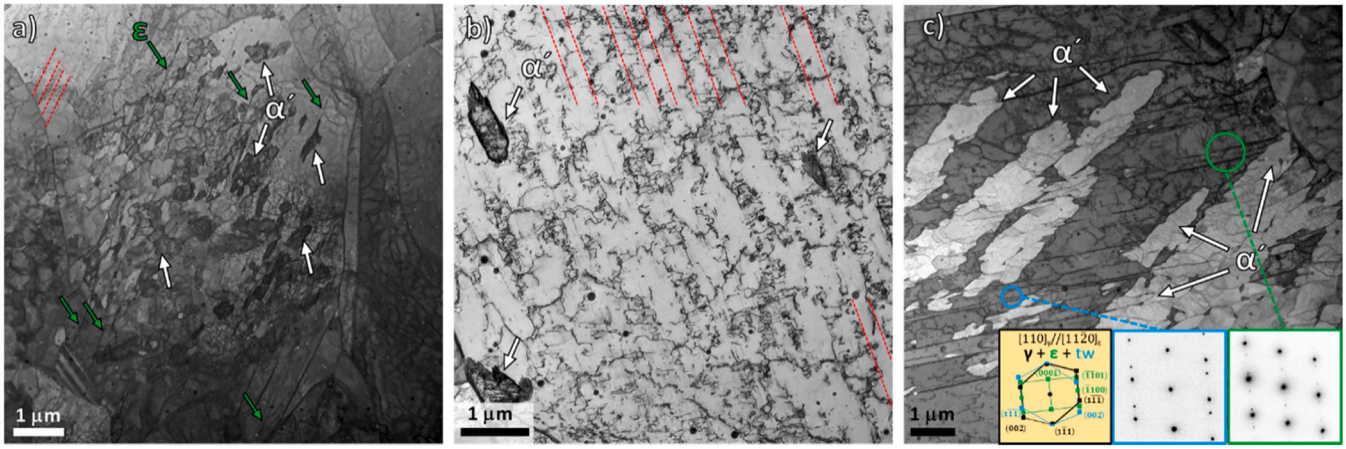

Fig. 9. Post mortem STEM BF images of the microstructure after cyclic straining at $\varepsilon_a = 1\%$: a) complex structure containing PSBs, narrow bands of ε-martensite with embedded α′-martensite nuclei and large α′-martensite islands; b) heavily modified cell dislocation microstructure with numerous PSBs (highlighted by red dashed lines); c) evidence of intensively deformed grain by concurrent deformation mechanisms resulting in α′-martensite clusters, fine bands of ε-martensite (yellow circle) and deformation twins (light blue circle) identified by SAED.

micrograph of a grain with combined activity of multiple deformation mechanisms, such as SIMT and deformation twinning. Moreover, several islands of α′-martensite accompanied by ε-martensite bands indicate active γ → ε → α′ transformation sequence. In general, the performed observations revealed diverse deformation microstructures within individual grains while some of them contained nearly intact dislocation cell structure. Such heterogeneity can be attributed to different effective strain amplitudes acting on individual grains stemming from various crystallographic orientations with respect to the LD, diverse local stress states and locally different intergranular interactions. The presence of significant effective plastic strain amplitude scatter was previously experimentally confirmed by Jiang [76] and Nellessen et al. [77]. Our observations indicated two grain fractions – i) the grains subjected to lower effective plastic strain amplitude resulting in less intensive cyclic plasticity and ii) the grains which experienced intensive cyclic plastic deformation upon high effective strain amplitudes. Fig. 9b presents the characteristic deformation microstructure of the first-mentioned grain fraction. Distinct similarities with microstructures typical for the cyclic tests held at $\varepsilon_a = 0.3\%$ (Fig. 7) and 0.5% (Fig. 8) were observed. The PSBs were the most frequent deformation microstructure feature, however, their frequency within individual grains was distinctively higher than after the tests held at lower ε_a, which complies well with generally accepted assumption that a PSB possesses a limited capacity of plastic deformation accommodation [78]. Observed martensite islands were still restricted within PSBs. In the case of intensively deformed grain fraction, large clusters of strain-induced α′-martensite aligned along active slip system, as shown in Fig. 9c, were found to be the characteristic evidence of intensive cyclic straining. Additionally, numerous planar features along the secondary slip system were observed in the regions between the α′-martensite clusters and were identified by SAED as ε-martensite and deformation twins. The deformation twinning was previously documented by Cui et al. [35,36] just in severely deformed areas in the vicinity of fatigue cracks, however, our TEM observations were performed more than 3 mm away from the fracture surface. It has been reported by Byun [79] and Woo et al. [32] that critical twinning stress is around 840 MPa for 316L SS, a similar steel grade to 304L. This value is above the nominal stress amplitudes of our LCF tests (approximately 500 – 600 MPa) but presumably possible to be reached with the contribution of local stress concentrations by intergranular interactions. Based on the observed microstructural evolution in the early stages of fatigue life (Section 3.3.1), it can be concluded that the deformation processes started with the PSBs formation followed by α′-martensite nucleation in their interior. The further growth of martensite islands led to the occurrence of large α′ clusters. Such complex microstructure resulted in difficult dislocation motion on the secondary slip system inducing subsequently stress concentrations due to dislocation pile-ups. This situation could locally trigger deformation twinning and γ → ε transformation, which was confirmed by SAED in Fig. 9c. The nucleation of the ε-martensite and deformation twins contributes to progressive fragmentation of microstructure, reducing further the dislocation mean free path. The proposed sequence of deformation mechanisms enhances a dynamic Hall-Petch effect reflected by the recorded cyclic hardening in later fatigue life stages. Contrary to that, cyclic loading at low ε_a presents significantly lower cyclic plastic deformation which is predominantly accommodated by PSBs. Since PSBs facilitate dislocation motion by ongoing gradual degradation of dislocation cell walls, the macroscopical response is cyclic softening. At later stages of fatigue life, the SIM nucleates in small extent within PSBs but the strengthening effect is not enough to cause cyclic hardening and results just in the weakening of cyclic softening or the appearance of cyclic saturation.

3.3.3. Martensite nucleation site characterization

The previous sections underlined the importance of the SIMT on cyclic behaviour as the principal contributor of the cyclic hardening stage. The conventional 304L SS is well-known for susceptibility to the TRIP effect under monotonic [80,81] and cyclic loading [26,61,65,82]. However, it has been reported by multiple studies that AM counterparts retained this ability predominantly upon monotonic loading [14,16,83]. On the other hand, the studies published by Zhang et al. [34,84,85] were dealing with the effect of cyclic loading on microstructure and reported an absence of α′-martensite even in the imminent vicinity of fracture surface. The distinct cyclic hardening of L-PBF 304L SS accompanied by the SIMT has been reported only by Pegues et al. [37]. The TRIP effect mitigation can be attributed to several jointly acting factors: i) unfavourable initial chemical composition of utilized powder, especially Cr/Ni ratio; ii) the powder gas atomization processing in nitrogen atmosphere can result in notable nitrogen uptake [86] causing a significant decrease of characteristic temperatures M_s and M_{d30}, which makes the TRIP effect less likely to occur [87]; iii) fine cell dislocation structure presents a grain size effect suppressing the SIMT; iv) high structural porosity can lead to a significant shortening of the fatigue crack initiation process and premature failures before the cyclic hardening stage is reached. The latter is documented in Fig. 10 by cyclic behaviour comparison of L-PBF 304L SS of various porosity fabricated by different process parameters from the identical powder. The accelerated fatigue crack initiation of the 304L with higher porosity resulted in premature failure without reaching significant cyclic hardening. Similar cyclic behaviour has been frequently recorded by other studies [36,69]. The low porosity specimens, utilized in this study, have shown higher resistance to the fatigue crack initiation. The cyclic strain localization in the vicinity of a crack tip and pores is avoided and cyclic plasticity is distributed along the whole specimen gauge area for a distinctively longer portion of fatigue life. That results in stronger SIMT along with other strengthening mechanisms described in the previous sections. The following paragraphs will characterize in detail the martensite phase distribution within the microstructure.

Fig. 11 presents the α′-martensite distribution within the solidification structure cyclically strained at $\varepsilon_a = 0.7\%$. The EBSD phase map, Fig. 11a, presents several melt pools, which were tentatively identified and highlighted according to the areas with high geometrically necessary dislocation (GND) density (see Fig. 11b) and characteristic radial grain alignment. A fraction of α′-martensite was located along the melt pool boundaries in a form of elongated clusters spanning across several grains. Such martensite arrangement suggests a certain relation with pronounced chemical segregation during the melt pool solidification process. Fig. 11c depicts STEM BF micrograph of melt pool boundary area densely occupied by α′-martensite. The EDS mapping of the area,

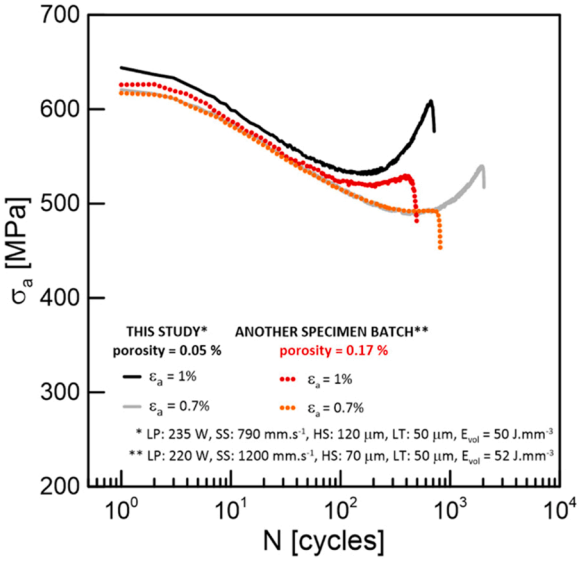

Fig. 10. Effect of higher structural porosity on cyclic behaviour. (LP – laser power; SS – scanning speed; HS – hatch spacing; LT – layer thickness; E_{vol} – volume energy density).

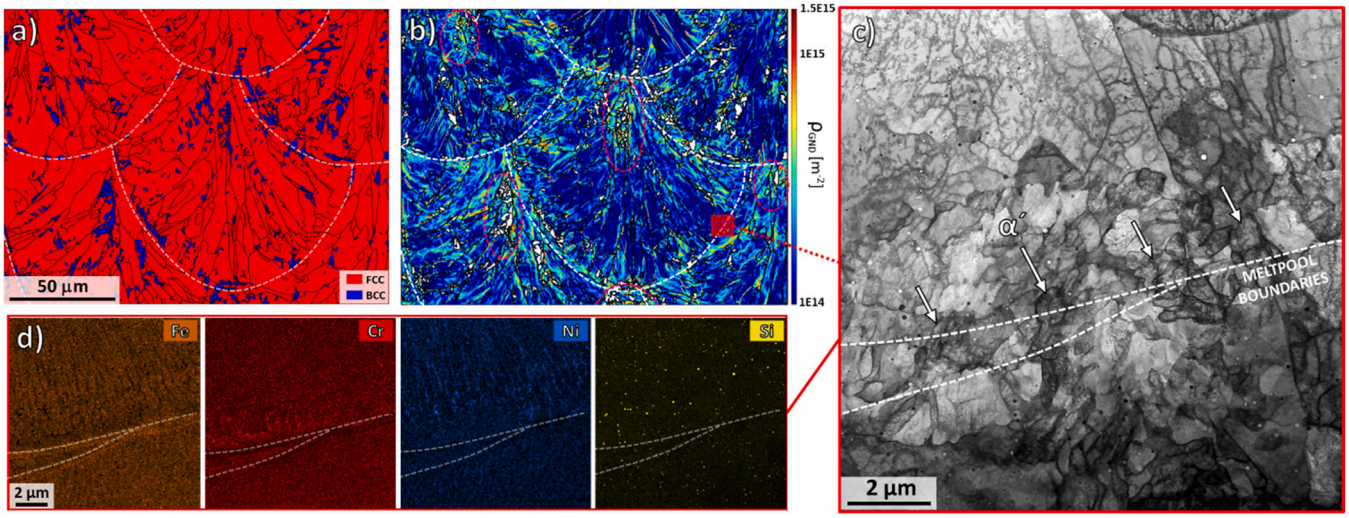

Fig. 11. Martensite distribution in microstructure after cyclic loading at $\varepsilon_a = 0.7\%$: a) EBSD phase map with highlighted melt pool boundaries (white dashed line); b) GND map showing the correlation of the α-martensite distribution and the areas with high GND density; c) STEM-BF image of melt pool boundary area; d) STEM EDS mapping.

Fig. 11d, indicated a notable Cr and Ni depletion along the melt pool boundary. This microstructural variety, and also higher GND density, can be ascribed to distinctively higher cooling rates at the onset of melt pool solidification. The solidification process initially tends to push alloying elements in front of the solidification front. Consequently, Fe content was higher along melt pool boundaries than in the interior where the Cr- and Ni-rich/Fe-depleted areas along cell dislocation walls are usually observed [17,33,88]. The authors assume that the local Cr and Ni depletion may contribute to local higher austenite metastability, i.e. lower SFE. Furthermore, the high GND density areas indirectly decrease the SFE based on the investigation of Woo et al. [32] which indicated SFE decline with increasing true strain of tensile loading. Therefore, the melt pool boundaries can be regarded as one of the preferential martensite transformation areas which are activated by cyclic plastic deformation. Additionally, the central areas of melt pool, highlighted in Fig. 11b, appear to also possess the increased SIMT susceptibility due to high GND density stemming from the final stage of melt pool solidification where growing dendritic grains were approaching each other along different orientations resulting in higher internal stresses and notable elemental segregation. The described solidification process-related martensite distribution indicates the important role of chemical segregation and internal dislocation substructure in the facilitation of the TRIP effect since intensive cyclic plastic straining is not the sole actuator of the process. Therefore, α′-martensite can occur even in grains with below-average Schmid factor values for perfect or partial dislocations, as is shown in Fig. S2 in Supplementary materials.

Fig. 12 presents the observed $\gamma \rightarrow \alpha'$ transformation on a much smaller scale than shown in Fig. 11. The STEM BF micrograph, inset of Fig. 7, shows a grain interior with a characteristic cell substructure and three well-developed PSBs aligned along the favourable slip system. The image depicts a striking difference in dislocation density between PSBs interior and austenite matrix. Although the residues of dislocation cell walls are still partially visible inside PSBs, they are characterized by very low dislocation density. This implies that their role as an effective barrier for dislocation motion has seriously decreased and, thus, it is expected that the Hall-Petch effect of the cell substructure is no longer relevant within PSBs. Therefore, such microstructure consists of a matrix, where dislocation motion is severely inhibited by well-preserved dislocation walls, and PSBs with favourable conditions for cyclic plastic deformation mediated by mobile dislocations. Moreover, it is assumed that the grain size dependence of the transformation induced plasticity (TRIP), previously reported by Sohrabi et al. [89] and Shen et al. [90] in conventional austenitic steels, is notably weakened by the significant local decrease of dislocation density in cell walls at intersections with PSBs. Consequently, the areas with intensive localization of cyclic plastic deformation, such as PSBs, PSB-PSB, and PSB-HAGB intersections, generally present favourable sites for the SIMT. The elemental EDS maps of Fig. 12 document microsegregation, where the cell wall areas are characterized by Cr and Ni enrichment, whereas the cell interiors are depleted of these elements. Such compositional

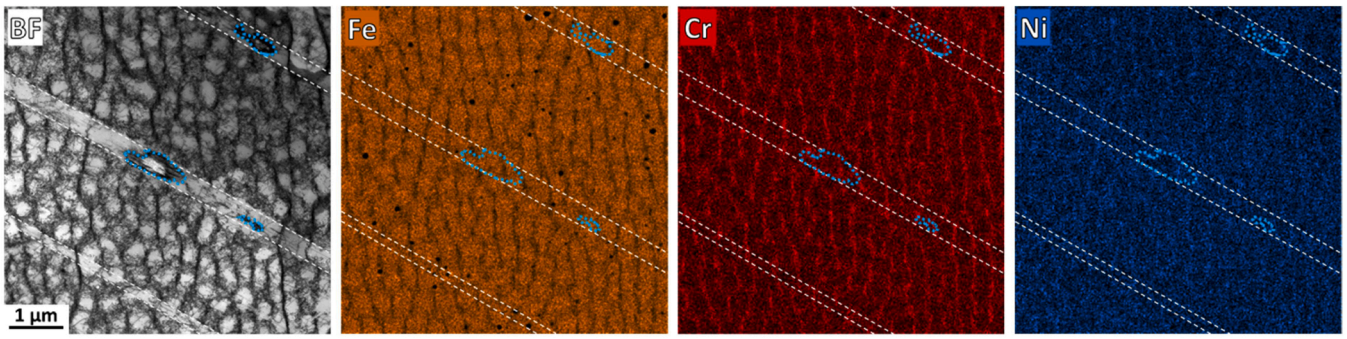

Fig. 12. STEM BF image of PSBs containing nuclei of α′-martensite within a grain located in the meltpool interior. STEM EDS mapping gives clear evidence that chemical microsegregation at dislocation cell size scale is not affected by cyclic plastic deformation contrary to diminished dislocation cell walls. α′-martensite nuclei were found be pinned between the areas of higher concentration of Cr.

fluctuations naturally introduce SFE irregularities and can affect martensite nucleation. It has been proposed by Kim et al. [33] that the martensite nucleates most likely from cell interiors where alloying element depletion results in slightly higher austenite metastability. The position and shape of martensite nuclei in Fig. 12 tend to exhibit certain variations with respect to Cr- and Ni-rich areas, supporting further this hypothesis.

In summary, the observed cyclic behaviour indicates superior cyclic strength in comparison to 304L SS conventionally produced counterparts, which is predefined by the hierarchical nature of L-PBF structure with a high degree of heterogeneity. High dislocation density already in as-built condition determines that an L-PBF structure exhibits the initial cyclic softening accompanied by the occurrence of PSBs, a dislocation spatial arrangement with significantly lower dislocation density. Cyclic plasticity during further cyclic straining was predominantly accommodated in PSBs, which subsequently led to the SIMT. With increasing ε_a, the α′-martensite volume fraction increased as well as deformation twinning. Therefore, the microstructure is progressively more complex, which reduces the mean free dislocation path. This microstructural evolution can be linked with the observed cyclic hardening. The EBSD and EDS mapping showed that martensite distribution strongly depends on the character of solidification structure, namely on the local compositional and GND density fluctuations. Therefore, these findings tend to indicate a possibility to modify the TRIP effect magnitude, by the processing parameters modifications. Especially, the mitigation or enhancement of chemical microsegregation or the modifications of cell size present promising routes towards the tailoring of materials cyclic behaviour. However, for any further fatigue performance enhancement and/or cyclic behaviour modification, the porosity reduction is of utmost imporantance.

4. Conclusion

The present study comprehensively investigated the cyclic behaviour of metastable L-PBF 304L SS in close relation to the undergoing microstructural changes due to the pronounced cyclic strain localization into PSBs and subsequently with triggered SIMT. The main conclusions are drawn as follows:

1. The character of cyclic behaviour strongly depends on the subjected strain amplitude. The cyclic loading at low strain amplitudes ($\varepsilon_a < 0.5\%$) has led to cyclic softening eventually followed by cyclic saturation. In the case of cyclic loadings held at $\varepsilon_a \geq 0.5\%$, the pronounced cyclic hardening as the final fatigue life stage was observed.
2. For the first time in L-PBF solidification structure, the dislocation microstructure evolution under cyclic loading was revealed at the early stages of the fatigue life. Distinct signs of cyclic strain localization appeared already after 5 cycles and continued to develop into well-distinguishable planar dislocation arrangements, resembling PSBs, frequently observed in conventionally processed materials. Significantly decreased dislocation density and nearly diminished initial cellular structure, presumably due to the intensive mobile dislocation – cell walls dislocation interactions, were observed within PSBs interior.
3. Cyclic plastic strain localization within PSBs led to the triggering of the SIMT. The Rugged shape of α′-martensite nuclei, featured with numerous straight interfaces aligned parallel to active slip plane and occurrence of ε-martensite in the vicinity, suggests the phase transformation sequence $\gamma \rightarrow \varepsilon \rightarrow \alpha'$.
4. Feritscope measurements enabled to follow the SIMT kinetics of the cyclic loading held at high ε_a - the first traces of α′-martensite already appeared after 50 cycles. During further loading, a progressive increase of the α′-martensite volume fraction was recorded, which could be linked with the accelerated rate of α′-martensite nucleation. The rapid increase of the phase fraction during the later stages of fatigue life was attributed to the growth of α′-martensite nuclei. The results indicate that α′-martensite phase presents the pivotal factor for the cyclic hardening behaviour by creating additional obstacles for dislocation motion.
5. Post-mortem microstructure observation revealed a heterogeneous distribution of cyclic deformation. The cyclic strain localization into PSBs accompanied by numerous fine α′-martensite nuclei was typical for fatigue loading held at low strain amplitudes. With further increase of strain amplitude, higher PSBs frequency alongside with higher α′-martensite volume fraction and additional deformation mechanisms, such as deformation twinning and $\gamma \rightarrow \varepsilon$-martensite phase transformation, were observed. As a consequence, the cyclically strained L-PBF structure got gradually more complex, leading to considerable cyclic hardening.
6. The link between pronounced elemental segregation and the SIMT was found especially in the areas of melt pool boundaries where strong depletion of Ni and Cr was identified. Moreover, the Cr an Ni depletion within the cell structure seems to have a promoting effect on the martensite nucleation within PSBs.

CRediT authorship contribution statement

Luboš Náhlík: Writing – review & editing, Supervision, Resources. **Michal Jambor:** Writing – review & editing, Visualization, Methodology, Investigation, Data curation, Conceptualization. **Miroslav Šmíd:** Writing – review & editing, Writing – original draft, Visualization, Resources, Project administration, Investigation, Funding acquisition, Data curation, Conceptualization. **Daniel Koutný:** Writing – review & editing, Validation, Supervision, Methodology, Investigation. **Kateřina Neumannová:** Writing – review & editing, Visualization, Investigation, Data curation. **Zdeněk Chlup:** Writing – review & editing, Methodology, Investigation.

Declaration of Competing Interest

The authors declare that they have no known competing financial interests or personal relationships that could have appeared to influence the work reported in this paper.

Data Availability

Data will be made available on request.

Acknowledgement

The authors are grateful for the financial support of the Czech Science Foundation by the project 19-25571Y. CzechNanoLab project LM2018110 funded by MEYS CR is gratefully acknowledged for the infrastructure support of the measurements at CEITEC Nano Research Infrastructure. The authors would like to thank the support from European Union's Horizon 2020 research and innovation programme (H2020-WIDESPREAD-2018, SIRAMM) under grant agreement No 857124.

Appendix A. Supporting information

Supplementary data associated with this article can be found in the online version at doi:10.1016/j.addma.2023.103503.

References

[1] Y. Bai, J. Zhang, C. Zhao, C. Li, H. Wang, Dual interfacial characterization and property in multi-material selective laser melting of 316L stainless steel and C52400 copper alloy, Mater. Charact. 167 (2020), 110489.
[2] H. Gu, C. Wei, L. Li, Q. Han, R. Setchi, M. Ryan, Q. Li, Multi-physics modelling of molten pool development and track formation in multi-track, multi-layer and

multi-material selective laser melting, Int. J. Heat. Mass Transf. 151 (2020), 119458.
[3] J. Koopmann, J. Voigt, T. Niendorf, Additive manufacturing of a steel–ceramic multi-material by selective laser melting, Metall. Mater. Trans. B 50 (2) (2019) 1042–1051.
[4] B. Rankouhi, S. Jahani, F.E. Pfefferkorn, D.J. Thoma, Compositional grading of a 316L-Cu multi-material part using machine learning for the determination of selective laser melting process parameters, Addit. Manuf. 38 (2021), 101836.
[5] H. Gaub, Customization of mass-produced parts by combining injection molding and additive manufacturing with Industry 4.0 technologies, Reinf. Plast. 60 (6) (2016) 401–404.
[6] D. Jankovics, A. Barari, Customization of automotive structural components using additive manufacturing and topology optimization, IFAC-Pap. 52 (10) (2019) 212–217.
[7] R. Lachmayer, P.C. Gembarski, P. Gottwald, R.B. Lippert, The potential of product customization using technologies of additive manufacturing, in: J. Bellemare, S. Carrier, K. Nielsen, F.T. Piller (Eds.), Managing Complexity, Springer International Publishing, Cham, 2017, pp. 71–81.
[8] K.S. Prakash, T. Nancharaih, V.V.S. Rao, Additive manufacturing techniques in manufacturing -an overview, Mater. Today.: Proc. 5 (2, Part 1) (2018) 3873–3882.
[9] W.E. Frazier, Metal additive manufacturing: a review, J. Mater. Eng. Perform. 23 (6) (2014) 1917–1928.
[10] B. Blakey-Milner, P. Gradl, G. Snedden, M. Brooks, J. Pitot, E. Lopez, M. Leary, F. Berto, A. du Plessis, Metal additive manufacturing in aerospace: a review, Mater. Des. 209 (2021), 110008.
[11] L. Liu, Q. Ding, Y. Zhong, J. Zou, J. Wu, Y.-L. Chiu, J. Li, Z. Zhang, Q. Yu, Z. Shen, Dislocation network in additive manufactured steel breaks strength–ductility trade-off, Mater. Today 21 (4) (2018) 354–361.
[12] S. Chen, G. Ma, G. Wu, A. Godfrey, T. Huang, X. Huang, Strengthening mechanisms in selective laser melted 316L stainless steel, Mater. Sci. Eng.: A 832 (2022), 142434.
[13] T. Voisin, J.-B. Forien, A. Perron, S. Aubry, N. Bertin, A. Samanta, A. Baker, Y. M. Wang, New insights on cellular structures strengthening mechanisms and thermal stability of an austenitic stainless steel fabricated by laser powder-bed-fusion, Acta Mater. 203 (2021), 116476.
[14] Z. Zhu, W. Li, Q.B. Nguyen, X. An, W. Lu, Z. Li, F.L. Ng, S.M. Ling Nai, J. Wei, Enhanced strength–ductility synergy and transformation-induced plasticity of the selective laser melting fabricated 304L stainless steel, Addit. Manuf. 35 (2020), 101300.
[15] H. Zhang, C. Li, G. Yao, Y. Shi, Y. Zhang, Effect of annealing treatment on microstructure evolution and deformation behavior of 304L stainless steel made by laser powder bed fusion, Int. J. Plast. 155 (2022), 103335.
[16] E. Polatidis, J. Čapek, A. Arabi-Hashemi, C. Leinenbach, M. Strobl, High ductility and transformation-induced-plasticity in metastable stainless steel processed by selective laser melting with low power, Scr. Mater. 176 (2020) 53–57.
[17] Y.M. Wang, T. Voisin, J.T. McKeown, J. Ye, N.P. Calta, Z. Li, Z. Zeng, Y. Zhang, W. Chen, T.T. Roehling, R.T. Ott, M.K. Santala, Philip J. Depond, M.J. Matthews, A. V. Hamza, T. Zhu, , Additively manufactured hierarchical stainless steels with high strength and ductility, Nat. Mater. 17 (1) (2018) 63–71.
[18] D. Kong, C. Dong, S. Wei, X. Ni, L. Zhang, R. Li, L. Wang, C. Man, X. Li, About metastable cellular structure in additively manufactured austenitic stainless steels, Addit. Manuf. 38 (2021), 101804.
[19] T.R. Smith, J.D. Sugar, C. San Marchi, J.M. Schoenung, Strengthening mechanisms in directed energy deposited austenitic stainless steel, Acta Mater. 164 (2019) 728–740.
[20] M. Seleznev, R. Wagner, A. Weidner, M. Wendler, O. Volkova, H. Biermann, Direct tuning of the microstructural and mechanical properties of high-alloy austenitic steel by electron beam melting, Addit. Manuf. 47 (2021), 102253.
[21] J. Günther, R. Lehnert, R. Wagner, C. Burkhardt, M. Wendler, O. Volkova, H. Biermann, T. Niendorf, Effect of compositional variation induced by EBM processing on deformation behavior and phase stability of austenitic Cr-Mn-Ni TRIP steel, JOM 72 (3) (2020) 1052–1064.
[22] D.T. Pierce, J.A. Jiménez, J. Bentley, D. Raabe, J.E. Wittig, The influence of stacking fault energy on the microstructural and strain-hardening evolution of Fe–Mn–Al–Si steels during tensile deformation, Acta Mater. 100 (2015) 178–190.
[23] A. Glage, A. Weidner, H. Biermann, Cyclic deformation behaviour of three austenitic cast CrMnNi TRIP/TWIP steels with various Ni content, Steel Res. Int. 82 (9) (2011) 1040–1047.
[24] U. Krupp, H.J. Christ, P. Lezuo, H.J. Maier, R.G. Teteruk, Influence of carbon concentration on martensitic transformation in metastable austenitic steels under cyclic loading conditions, Mater. Sci. Eng.: A 319–321 (2001) 527–530.
[25] U. Krupp, C. West, H.J. Christ, Deformation-induced martensite formation during cyclic deformation of metastable austenitic steel: Influence of temperature and carbon content, Mater. Sci. Eng.: A 481–482 (2008) 713–717.
[26] J. Man, M. Smaga, I. Kubèna, D. Eifler, J. Polák, Effect of metallurgical variables on the austenite stability in fatigued AISI 304 type steels, Eng. Fract. Mech. 185 (2017) 139–159.
[27] C.W. Shao, P. Zhang, R. Liu, Z.J. Zhang, J.C. Pang, Z.F. Zhang, Low-cycle and extremely-low-cycle fatigue behaviors of high-Mn austenitic TRIP/TWIP alloys: Property evaluation, damage mechanisms and life prediction, Acta Mater. 103 (2016) 781–795.
[28] Y. Kim, W. Choi, H. Choo, K. An, H.-S. Choi, S.Y. Lee, In situ neutron diffraction study of phase transformation of high Mn steel with different carbon content, Crystals 10 (2020) 101.
[29] C. Bean, F. Wang, M.A. Charpagne, P. Villechaise, V. Valle, S.R. Agnew, D. S. Gianola, T.M. Pollock, J.C. Stinville, Heterogeneous slip localization in an additively manufactured 316L stainless steel, Int. J. Plast. 159 (2022), 103436.
[30] Z. Sun, X. Tan, S.B. Tor, C.K. Chua, Simultaneously enhanced strength and ductility for 3D-printed stainless steel 316L by selective laser melting, NPG Asia Mater. 10 (4) (2018) 127–136.
[31] X. Ni, D. Kong, W. Wu, L. Zhang, C. Dong, Deformation-induced martensitic transformation in 316L stainless steels fabricated by laser powder bed fusion, Mater. Lett. 302 (2021), 130377.
[32] W. Woo, J.S. Jeong, D.K. Kim, C.M. Lee, S.H. Choi, J.Y. Suh, S.Y. Lee, S. Harjo, T. Kawasaki, Stacking fault energy analyses of additively manufactured stainless steel 316L and CrCoNi medium entropy alloy using in situ neutron diffraction, Sci. Rep. 10 (1) (2020) 1350.
[33] J.-M. Kim, H.-H. Jin, J. Kwon, S.H. Kang, B.-S. Lee, Effects of cellular segregation for high strength and ductility of additively manufactured 304L stainless steel, Mater. Charact. 194 (2022), 112364.
[34] H. Zhang, M. Xu, P. Kumar, C. Li, W. Dai, Z. Liu, Z. Li, Y. Zhang, Enhancement of fatigue resistance of additively manufactured 304L SS by unique heterogeneous microstructure, Virtual Phys. Prototyp. 16 (2) (2021) 125–145.
[35] L. Cui, D. Deng, F. Jiang, R.L. Peng, T. Xin, R.T. Mousavian, Z. Yang, J. Moverare, Superior low cycle fatigue property from cell structures in additively manufactured 316L stainless steel, J. Mater. Sci. Technol. 111 (2022) 268–278.
[36] L. Cui, F. Jiang, D. Deng, T. Xin, X. Sun, R.T. Mousavian, R.L. Peng, Z. Yang, J. Moverare, Cyclic response of additive manufactured 316L stainless steel: The role of cell structures, Scr. Mater. 205 (2021), 114190.
[37] J.W. Pegues, M.D. Roach, N. Shamsaei, Additive manufacturing of fatigue resistant austenitic stainless steels by understanding process-structure–property relationships, Mater. Res. Lett. 8 (1) (2020) 8–15.
[38] L. Cui, S. Jiang, J. Xu, R.L. Peng, R.T. Mousavian, J. Moverare, Revealing relationships between microstructure and hardening nature of additively manufactured 316L stainless steel, Mater. Des. 198 (2021), 109385.
[39] H. Zhang, C. Li, Y. Shi, G. Yao, Y. Zhang, Fatigue and tensile deformation behaviors of laser powder bed fused 304L austenitic stainless steel, Mater. Sci. Eng.: A 849 (2022), 143503.
[40] J.A. Cherry, H.M. Davies, S. Mehmood, N.P. Lavery, S.G.R. Brown, J. Sienz, Investigation into the effect of process parameters on microstructural and physical properties of 316L stainless steel parts by selective laser melting, Int. J. Adv. Manuf. Technol. 76 (5) (2015) 869–879.
[41] C. Sofras, J. Čapek, A. Arabi-Hashemi, C. Leinenbach, M. Frost, K. An, R.E. Logé, M. Strobl, E. Polatidis, Tailored deformation behavior of 304L stainless steel through control of the crystallographic texture with laser-powder bed fusion, Mater. Des. 219 (2022), 110789.
[42] Q.B. Nguyen, Z. Zhu, F.L. Ng, B.W. Chua, S.M.L. Nai, J. Wei, High mechanical strengths and ductility of stainless steel 304L fabricated using selective laser melting, J. Mater. Sci. Technol. 35 (2) (2019) 388–394.
[43] R.E. Schramm, R.P. Reed, Stacking fault energies of seven commercial austenitic stainless steels, Metall. Trans. A 6 (7) (1975) 1345.
[44] C.A. Schneider, W.S. Rasband, K.W. Eliceiri, NIH Image to ImageJ: 25 years of image analysis, Nat. Methods 9 (7) (2012) 671–675.
[45] R. Hielscher, H. Schaeben, A novel pole figure inversion method: specification of the MTEX algorithm, J. Appl. Crystallogr. 41 (6) (2008) 1024–1037.
[46] J. Talonen, P. Aspegren, H. Hänninen, Comparison of different methods for measuring strain induced α-martensite content in austenitic steels, Mater. Sci. Technol. 20 (12) (2004) 1506–1512.
[47] Y. Li, D. Yu, B. Li, X. Chen, Martensitic transformation of an austenitic stainless steel under non-proportional cyclic loading, Int. J. Fatigue 124 (2019) 338–347.
[48] K. Guan, Z. Wang, M. Gao, X. Li, X. Zeng, Effects of processing parameters on tensile properties of selective laser melted 304 stainless steel, Mater. Des. 50 (2013) 581–586.
[49] S.R. Narasimharaju, W. Zeng, T.L. See, Z. Zhu, P. Scott, X. Jiang, S. Lou, A comprehensive review on laser powder bed fusion of steels: processing, microstructure, defects and control methods, mechanical properties, current challenges and future trends, J. Manuf. Process. 75 (2022) 375–414.
[50] H.L. Wei, J. Mazumder, T. DebRoy, Evolution of solidification texture during additive manufacturing, Sci. Rep. 5 (1) (2015) 16446.
[51] O. Andreau, I. Koutiri, P. Peyre, J.-D. Penot, N. Saintier, E. Pessard, T. De Terris, C. Dupuy, T. Baudin, Texture control of 316L parts by modulation of the melt pool morphology in selective laser melting, J. Mater. Process. Technol. 264 (2019) 21–31.
[52] S. Katayama, A. Matsunawa, Solidification microstructure of laser welded stainless steels, Int. Congr. Appl. Lasers Electro-Opt. 1984 (2) (1984) 60–67.
[53] P. Köhnen, M. Létang, M. Voshage, J.H. Schleifenbaum, C. Haase, Understanding the process-microstructure correlations for tailoring the mechanical properties of L-PBF produced austenitic advanced high strength steel, Addit. Manuf. 30 (2019), 100914.
[54] K. Saeidi, L. Kvetková, F. Lofaj, Z. Shen, Austenitic stainless steel strengthened by the in situ formation of oxide nanoinclusions, RSC Adv. 5 (27) (2015) 20747–20750.
[55] P. Deng, M. Karadge, R.B. Rebak, V.K. Gupta, B.C. Prorok, X. Lou, The origin and formation of oxygen inclusions in austenitic stainless steels manufactured by laser powder bed fusion, Addit. Manuf. 35 (2020), 101334.
[56] L. Cui, F. Jiang, R.L. Peng, R.T. Mousavian, Z. Yang, J. Moverare, Dependence of microstructures on fatigue performance of polycrystals: a comparative study of conventional and additively manufactured 316L stainless steel, Int. J. Plast. 149 (2022), 103172.

[57] O.O. Salman, C. Gammer, A.K. Chaubey, J. Eckert, S. Scudino, Effect of heat treatment on microstructure and mechanical properties of 316L steel synthesized by selective laser melting, Mater. Sci. Eng.: A 748 (2019) 205–212.
[58] Z.G. Zhu, X.H. An, W.J. Lu, Z.M. Li, F.L. Ng, X.Z. Liao, U. Ramamurty, S.M.L. Nai, J. Wei, Selective laser melting enabling the hierarchically heterogeneous microstructure and excellent mechanical properties in an interstitial solute strengthened high entropy alloy, Mater. Res. Lett. 7 (11) (2019) 453–459.
[59] A.E. Wilson-Heid, S. Qin, A.M. Beese, Multiaxial plasticity and fracture behavior of stainless steel 316L by laser powder bed fusion: Experiments and computational modeling, Acta Mater. 199 (2020) 578–592.
[60] J.H. Rao, Y. Zhang, X. Fang, Y. Chen, X. Wu, C.H.J. Davies, The origins for tensile properties of selective laser melted aluminium alloy A357, Addit. Manuf. 17 (2017) 113–122.
[61] M. Šmíd, I. Kuběna, M. Jambor, S. Fintová, Effect of solution annealing on low cycle fatigue of 304L stainless steel, Mater. Sci. Eng.: A, 824 (2021) 141807.
[62] R. Alain, P. Violan, J. Mendez, Low cycle fatigue behavior in vacuum of a 316L type austenitic stainless steel between 20 and 600°C Part I: fatigue resistance and cyclic behavior, Mater. Sci. Eng.: A 229 (1) (1997) 87–94.
[63] M.S. Pham, S.R. Holdsworth, K.G.F. Janssens, E. Mazza, Cyclic deformation response of AISI 316L at room temperature: Mechanical behaviour, microstructural evolution, physically-based evolutionary constitutive modelling, Int. J. Plast. 47 (2013) 143–164.
[64] J. Zhou, Z. Sun, P. Kanouté, D. Retraint, Experimental analysis and constitutive modelling of cyclic behaviour of 316L steels including hardening/softening and strain range memory effect in LCF regime, Int. J. Plast. 107 (2018) 54–78.
[65] M. Bayerlein, H.J. Christ, H. Mughrabi, Plasticity-induced martensitic transformation during cyclic deformation of AISI 304L stainless steel, Mater. Sci. Eng.: A 114 (1989) L11–L16.
[66] H. Mughrabi, The cyclic hardening and saturation behaviour of copper single crystals, Mater. Sci. Eng. 33 (2) (1978) 207–223.
[67] P. Lukáš, L. Kunz, Role of persistent slip bands in fatigue, Philos. Mag. 84 (3–5) (2004) 317–330.
[68] S. Lavenstein, Y. Gu, D. Madisetti, J.A. El-Awady, The heterogeneity of persistent slip band nucleation and evolution in metals at the micrometer scale, Science 370 (6513) (2020) eabb2690.
[69] C.-H. Yu, A. Leicht, R.L. Peng, J. Moverare, Low cycle fatigue of additively manufactured thin-walled stainless steel 316L, Mater. Sci. Eng.: A 821 (2021), 141598.
[70] Y. Chen, X. Wang, J. shen, Y. Peng, Y. Jiang, X. Yang, S.B. Leen, J. Gong, Deformation mechanisms of selective laser melted 316L austenitic stainless steel in high temperature low cycle fatigue, Mater. Sci. Eng.: A 843 (2022), 143123.
[71] M. Hollmann, J. Bretschneider, C. Holste, Dislocation structure and strain localisation in nickel single crystals cyclically deformed at 77 K, Cryst. Res. Technol. 35 (4) (2000) 479–492.
[72] M. Kumagai, M. Kuroda, T. Matsuno, S. Harjo, K. Akita, In situ neutron diffraction analysis of microstructural evolution-dependent stress response in austenitic stainless steel under cyclic plastic deformation, Mater. Des. 221 (2022), 110965.
[73] G.B. Olson, M. Cohen, A mechanism for the strain-induced nucleation of martensitic transformations, J. Less Common Met. 28 (1) (1972) 107–118.
[74] E. Polatidis, W.N. Hsu, M. Šmíd, T. Panzner, S. Chakrabarty, P. Pant, H. Van Swygenhoven, Suppressed martensitic transformation under biaxial loading in low stacking fault energy metastable austenitic steels, Scr. Mater. 147 (2018) 27–32.
[75] D. Jang, C. Cai, J.R. Greer, Influence of homogeneous interfaces on the strength of 500 nm diameter Cu nanopillars, Nano Lett. 11 (4) (2011) 1743–1746.
[76] Y. Jiang, An experimental study of inhomogeneous cyclic plastic deformation, J. Eng. Mater. Technol. 123 (3) (2001) 274–280.
[77] J. Nellessen, S. Sandlöbes, D. Raabe, Effects of strain amplitude, cycle number and orientation on low cycle fatigue microstructures in austenitic stainless steel studied by electron channelling contrast imaging, Acta Mater. 87 (2015) 86–99.
[78] F. Meng, E. Ferrié, C. Déprés, M. Fivel, 3D discrete dislocation dynamic investigations of persistent slip band formation in FCC metals under cyclical deformation, Int. J. Fatigue 149 (2021), 106234.
[79] T.S. Byun, On the stress dependence of partial dislocation separation and deformation microstructure in austenitic stainless steels, Acta Mater. 51 (11) (2003) 3063–3071.
[80] S.S. Hecker, M.G. Stout, K.P. Staudhammer, J.L. Smith, Effects of strain state and strain rate on deformation-induced transformation in 304 stainless steel: part I. Magnetic measurements and mechanical behavior, Metall. Trans. A 13 (4) (1982) 619–626.
[81] M.G. Stout, P.S. Follansbee, Strain rate sensitivity, strain hardening, and yield behavior of 304L stainless steel, J. Eng. Mater. Technol. 108 (4) (1986) 344–353.
[82] J. Colin, A. Fatemi, S. Taheri, Cyclic hardening and fatigue behavior of stainless steel 304L, J. Mater. Sci. 46 (1) (2011) 145–154.
[83] P. Kumar, Z. Zhu, S.M.L. Nai, R.L. Narayan, U. Ramamurty, Fracture toughness of 304L austenitic stainless steel produced by laser powder bed fusion, Scr. Mater. 202 (2021), 114002.
[84] H. Zhang, C. Li, G. Yao, Y. Shi, Y. Zhang, Investigation of surface quality, microstructure, deformation mechanism, and fatigue performance of additively manufactured 304L stainless steel using grinding, Int. J. Fatigue 160 (2022), 106838.
[85] H. Zhang, M. Xu, Z. Liu, C. Li, P. Kumar, Z. Liu, Y. Zhang, Microstructure, surface quality, residual stress, fatigue behavior and damage mechanisms of selective laser melted 304L stainless steel considering building direction, Addit. Manuf. 46 (2021), 102147.
[86] C. Cui, V. Uhlenwinkel, A. Schulz, H.-W. Zoch, Austenitic stainless steel powders with increased nitrogen content for laser additive manufacturing, Metals 10 (2020) 61.
[87] L.E. Murr, E. Martinez, J. Hernandez, S. Collins, K.N. Amato, S.M. Gaytan, P. W. Shindo, Microstructures and properties of 17-4 PH stainless steel fabricated by selective laser melting, J. Mater. Res. Technol. 1 (3) (2012) 167–177.
[88] K.M. Bertsch, G. Meric de Bellefon, B. Kuehl, D.J. Thoma, Origin of dislocation structures in an additively manufactured austenitic stainless steel 316L, Acta Mater. 199 (2020) 19–33.
[89] M.J. Sohrabi, H. Mirzadeh, S. Sadeghpour, R. Mahmudi, Grain size dependent mechanical behavior and TRIP effect in a metastable austenitic stainless steel, Int. J. Plast. 160 (2023), 103502.
[90] Y.F. Shen, N. Jia, Y.D. Wang, X. Sun, L. Zuo, D. Raabe, Suppression of twinning and phase transformation in an ultrafine grained 2GPa strong metastable austenitic steel: experiment and simulation, Acta Mater. 97 (2015) 305–315.